Lecture 3: Microlensing of Quasar Broad Emission Lines
Case study: 18 image pairs in 16 lenses

Emilio E. Falco
Smithsonian Astrophysical Observatory
F. L. Whipple Observatory
670 Mt. Hopkins Rd.
Amado, AZ 85645, USA

Inspiration:
"Microlensing of Quasar Broad Emission Lines: Constraints on Broad Line Region Size"
E. Guerras et al. 2012, astro-ph/1207.2042 (EG12)

1. BROAD EMISSION LINES

Strong, broad emission lines are seen in many AGNs. An example is in Fig. 1. Their properties are useful diagnostics because of their proximity to the central engine and because they probe the gas flows either fueling the AGN or feeding mass and energy back into the host galaxy.

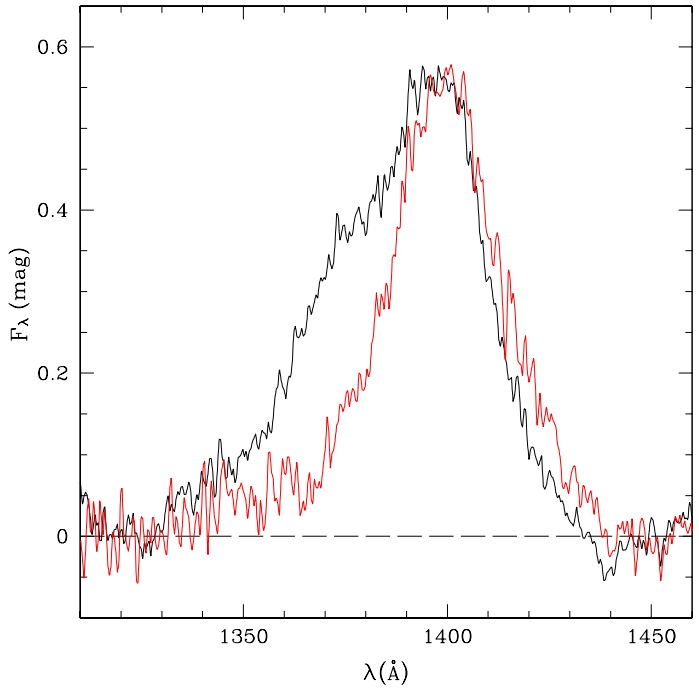

Fig. 1.— EG12: a detailed view of the differences in the SiIVλ1400 line profiles corresponding to the A and B images of SDSS J1004+4112 from Richards et al. (2004).

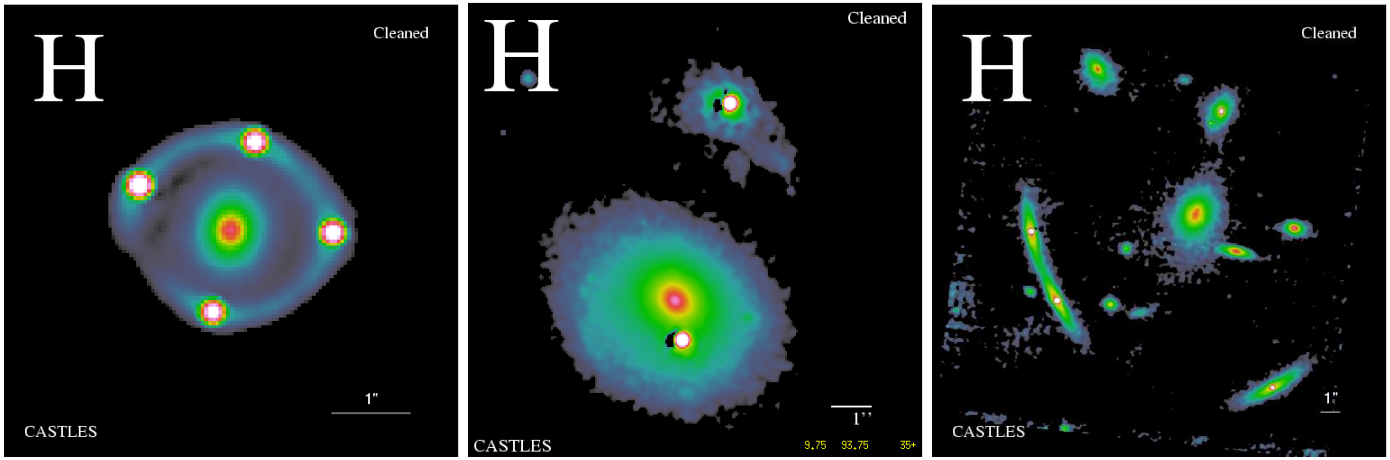

Fig. 2.— A sub-sample of EG12 targets for measuring BLR sizes. CASTLES H-band images of HE0435, Q0957 and SDSS1004.

A popular probe of the geometry and kinematics of broad line regions (BLRs) is reverberation mapping (RM), where the delayed response of the emission line flux to changes in the photoionizing continuum is used to estimate the distance of the line-emitting material from the central engine (Peterson 1993, 2006). RM measures the light travel time between the continuum and the BLR from the time lag between changes in their luminosities. Fig. 3 shows RM results for NGC 3227 ($cz \sim 1160$ km/s).

RM studies have shown that the global structure of the BLR is consistent with photoionization models, with the radius increasing with the square root of the continuum luminosity (e.g. Bentz et al. 2009) and high ionization lines (e.g. C IV) originating at smaller radii than low ionization lines (e.g. Hβ). Recent studies have increasingly focused on measuring the delays as a function of line velocity to understand the kinematics of the BLR (Denney et al. 2009, 2010, Bentz et al. 2010, Brewer et al. 2011, Doroshenko et al. 2012, Pancoast et al. 2012). The results to date suggest that there is no common kinematic structure, with different sources showing signs of inward, outward and disk-like velocity structures.

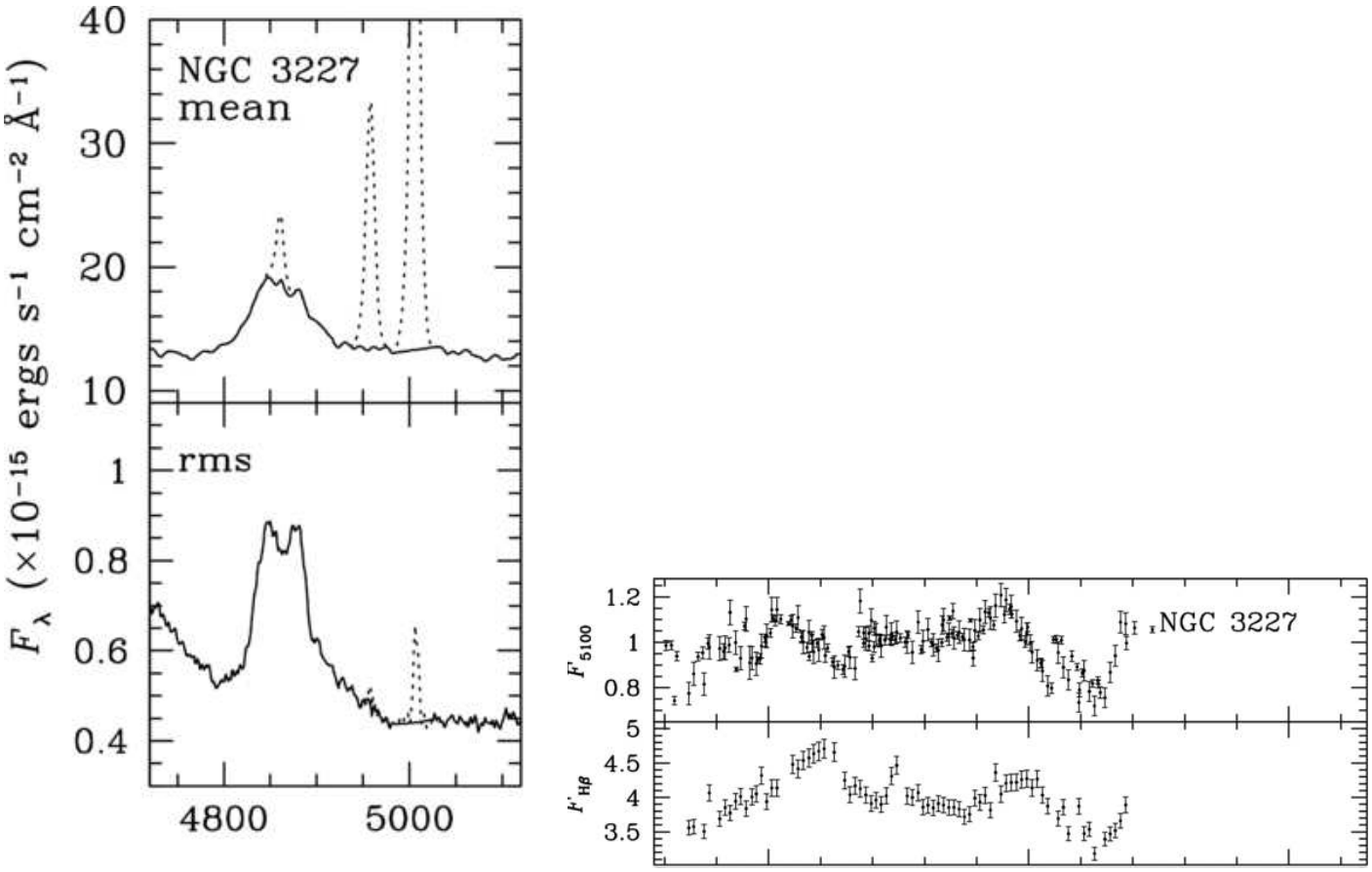

Fig. 3.— From Denney et al. 2009. Left: mean and RMS spectrum of NGC 3227 from MDM observations. The solid line shows the mean and RMS spectrum after removal of [O III] $\lambda\lambda 4959, 5007$ narrow emission lines. The dotted line is the spectrum prior to this subtraction. Right: lightcurves of the 5100 Å continuum (top panel) and Hβ emission-line flux (bottom panel) in units of 10^{15} erg/s/cm^2/Å and 10^{13} erg/s/cm^2/Å respectively, for NGC 3227.

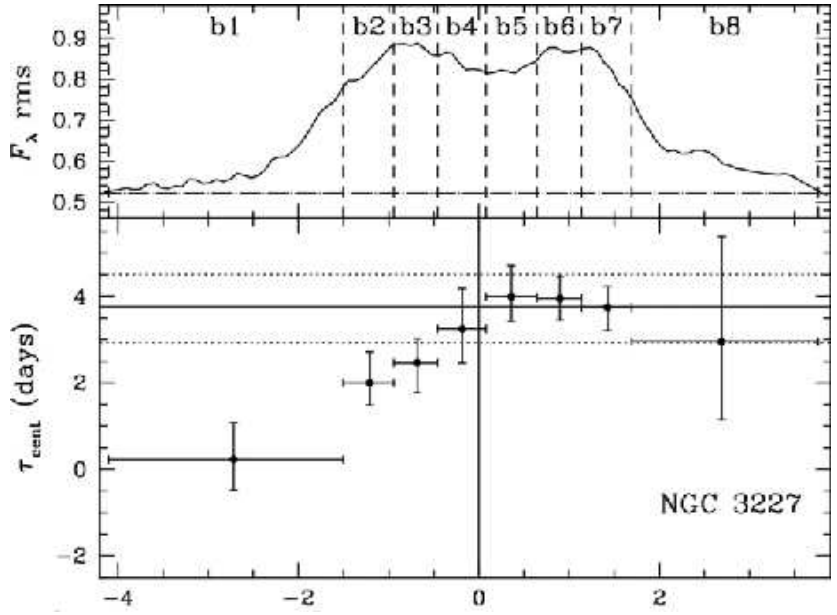

Fig. 4.— Division of the Hβ rms profile into equal-flux bins (top panel; vertical dashed lines), and corresponding velocity-resolved time-delay measurements (bottom panels) for NGC 3227. Delays are plotted at the flux centroid of each velocity bin. Error bars on the lag measurements in the velocity direction (bottom panels) reflect the bin size, with each bin labeled by number in the top panel. Negative (positive) velocities are blueshifts (redshifts) from the line center. The horizontal solid and dotted lines in the bottom panel show the mean BLR lag and associated errors, while the horizontal dot-dashed line in the top panel represents the linearly fit continuum level.

2. RM APPLICATIONS

1. RM studies are limited to nearby, lower-luminosity AGN because the delay times for distant, luminous quasars are long and additionally dilated by the redshift. High-z times are longer than existing monitoring programs can be sustained.

2. Higher-luminosity quasars have lower variability amplitudes (see, e.g., MacLeod et al. 2010).

3. One of the most important applications of RM is as a calibrator for estimating black hole (BH) masses from single-epoch spectra (Wandel et al. 1999). These calibrations use Hα and Hβ but the easiest lines to measure for high-redshift quasars are the Mg II and C IV lines because the Balmer lines move to the infrared. However, Assef et al. (2011) obtained BH mass estimates based on IR spectra of lensed quasars. They showed that Hα and Hβ yield consistent estimates with those from other emission lines.

3. MICROLENSING THE BLR

Stars in a lens galaxy can produce microlensing. They differentially magnify components of the quasar emission regions, leading to time and wavelength-dependent changes in the flux ratios of the images. Microlensing is thus a useful tool to study the structure of the BLR.

The amplitude of the microlensing magnification of lensed images depends on the size of the emission region: the smaller a region the larger its magnification. For some time, the BLR was considered too large to be affected by microlensing (Nemiroff 1988, Schneider & Wambsganss 1990), but for sizes consistent with RM, the BLRs should show microlensing variability as shown by observations (Mosquera & Kochanek 2011) and from theory, Abajas et al. (2002, 2007), Lewis & Ibata (2004) and Garsden et al (2011).

Observational evidence for microlensing in the BLR has been discussed for Q2237+0305 (Lewis et al. 1998, Metcalf et al. 2004, Wayth et al. 2005, Eigenbrod et al. 2008, O'Dowd et al. 2010, Sluse et al. 2011), SDSS J1004+4112 (Richards et al. 2004, Gómez-Álvarez et al. 2006, Lamer et al. 2006, Abajas et al. 2007) and SDSS J0924+0219 (Keeton et al. 2006), as well as in broader surveys by Sluse et al. (2012) and Motta et al. (2012). For example, in their detailed study of Q2237+0305, Sluse et al. (2011) demonstrated the power of microlensing, obtaining estimates of the BLR size for both CIII] ($r_{CIII]} \sim 49$ light-days) and C IV ($r_{CIV} \sim 66$ light-days) emission lines. Like RM, the microlensing size estimates can also be made as a function of velocity, and the two methods can even be combined to provide even more detailed constraints (Garsden et al. 2011).

4. GOALS

- Separate the effects of microlensing from those of the macro magnification, millilensing (e.g. Dalal & Kochanek 2002) and extinction (e.g. Motta et al. 2002).

- Use differential flux ratios between the cores and wings of the emission lines observed in two images

$$\Delta m = (m_1 - m_2)_{wings} - (m_1 - m_2)_{core}. \quad (1)$$

- Calculate magnitudes from the lines after subtraction of a linear continuum. Because the line emission regions are relatively compact and the wavelength differences are small, Δm removes the effects of the macro magnification, millilensing and extinction.

- Assume that the line core, defined by the velocity range $|\Delta v| < 850$ km/s, is not affected by microlensing compared to the wings. Existing velocity-resolved RM maps (e.g. Denney et al. 2009, 2010, Bentz et al. 2010, Barth et al. 2011, Pancoast et al. 2012) all find longer time delays in this velocity range, indicating that the material in the line core is at larger distances from the central engine. Sluse et al. (2011) also found this in their microlensing analysis of Q2237+0305. High velocity material must be near the central engine to have the observed Doppler shifts, but the low-velocity material is a mixture of material near the BH but moving perpendicular to the line of sight and material far from the BH with low radial velocity. Thus, the line core should generically be produced by material spread over a broader area and hence be significantly less microlensed than the line wings.

Figure 5 shows histograms of Δm for the low and high ionization lines, and the values are reported in Table 1. Even the largest microlensing effects are relatively small, with $|\Delta m| < 0.2$ mag. Also, more high ionization lines (6 of 14) than low ionization lines (2 of 14) show significantly non-zero Δm given the typical uncertainties (0.05 mag). The counting here includes only image pairs showing the anomalies, not the numbers of lines showing anomalies, so e.g. SDSSJ 1004+4112 with multiple high ionization anomalies is counted only once. Qualitatively, it is clear that both high and low ionization lines are weakly microlensed and that the low ionization lines arise from a larger source than the high ionization lines.

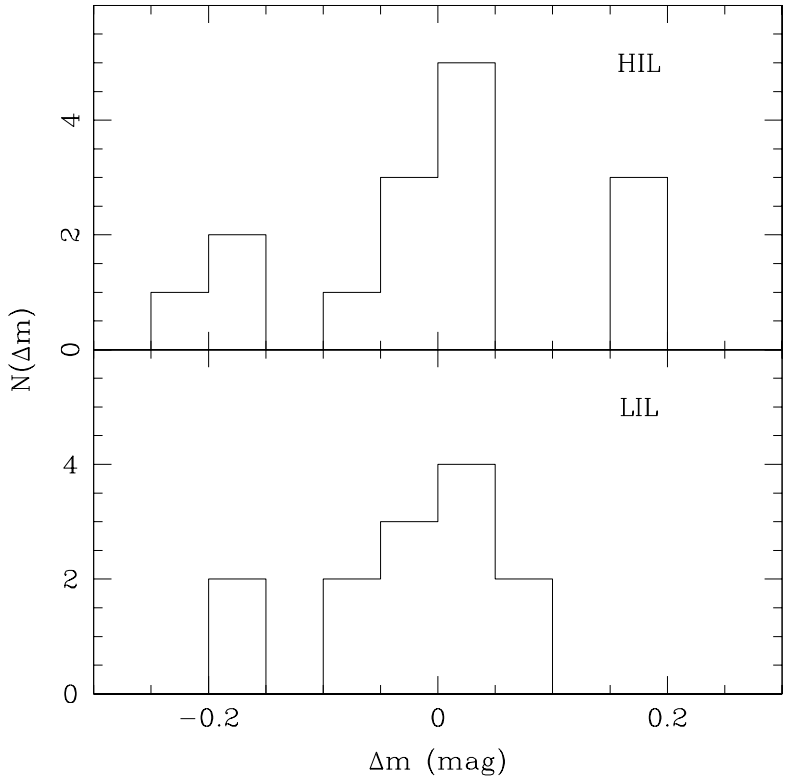

Fig. 5.— EG12: histograms of the microlensing magnifications, Δm, observed for the high (upper) and low (lower) ionization lines.

Given the estimates of the differential effects of microlensing on the core and wings of the emission lines, EG12 used Monte Carlo simulations to estimate the size of the emission regions. They assume that the line core emission regions are large enough that they are not microlensed, and model the wing emission regions as Gaussians. Mortonson et al. (2005) have shown that the effects of microlensing are determined by the projected half-light area of the source, and even with full microlensing light curves it is difficult to estimate the shape of the emission regions (see Poindexter & Kochanek (2010), Blackburne et al. (2011)).

EG12 used estimates of the dimensionless surface density κ and shear γ of the lens for each image from Mediavilla et al. (2009) or the updated values for SBS 0909+532 from Mediavilla et al. (2011a). They assumed that the fraction of the mass in stars is 5%. For a stellar mass of $M = 1M_{\odot}$, EG12 generated square magnification patterns for each image that were 1000 light-days across with a 0.5 light-day pixel scale using the Inverse Polygon Mapping algorithm (Mediavilla et al. 2006, 2011b). They calculated magnifications for a Gaussian source of size r_s ($I \propto \exp(-R^2/2r_s^2)$) by convolving the magnification pattern with the Gaussian. EG12 used a logarithmic grid of source sizes, $\ln r_s = 0.3 \times i$ for $i = 0, \cdots, 17$, where r_s is in light-days. The source sizes can be scaled to a different mean stellar mass as $r_s \propto (M/M_{\odot})^{1/2}$. EG12 followed a procedure similar to that used by Jiménez-Vicente et al. (2012) to estimate the average size of quasar accretion disks.

For any pair of images, EG12 generated the expected magnitude differences for a given source size by randomly drawing magnifications m_1 and m_2 from the convolved magnification pattern for the two images and taking the difference $\Delta m = m_1 - m_2$. The probability of observing a magnitude difference $\Delta m_{obs,k} \pm \sigma_k$ for lens/line k given

a source size r_s is then

$$p_k(r_s) \propto \sum_{l=1}^{N} \exp\left(-\frac{1}{2}\left(\frac{\Delta m_l - \Delta m_{obs,k}}{\sigma_k}\right)^2\right) \tag{2}$$

for $N = 10^8$ random trials at each source size. One can then estimate an average size for either the high or low ionization lines by combining the likelihoods

$$L(r_s) = \prod p_k(r_s) \tag{3}$$

for the individual lines. Implicitly we are also drawing magnifications for the core but assuming they are close enough to unity to be ignored.

Figure 6 shows the resulting likelihood functions for the high and low ionization lines. Simply using maximum likelihood estimation, we find 90% confidence estimates for the average sizes of the high and low ionization lines of $r_s = 24^{+22}_{-15}$ and $r_s = 55^{+150}_{-35}$ light-days, respectively. A rough estimate can be made of the consequences of ignoring microlensing of the line core by raising (lowering) the magnifications to represent anti-correlated (correlated) changes in the core relative to the line. The effects of uncorrelated changes will be intermediate to these limits. For a 20% amplitude, the central sizes shift over the range from $r_s = 20$ to 37 light-days for the high ionization lines and $r_s = 37$ to 120 light-days for the low ionization lines.

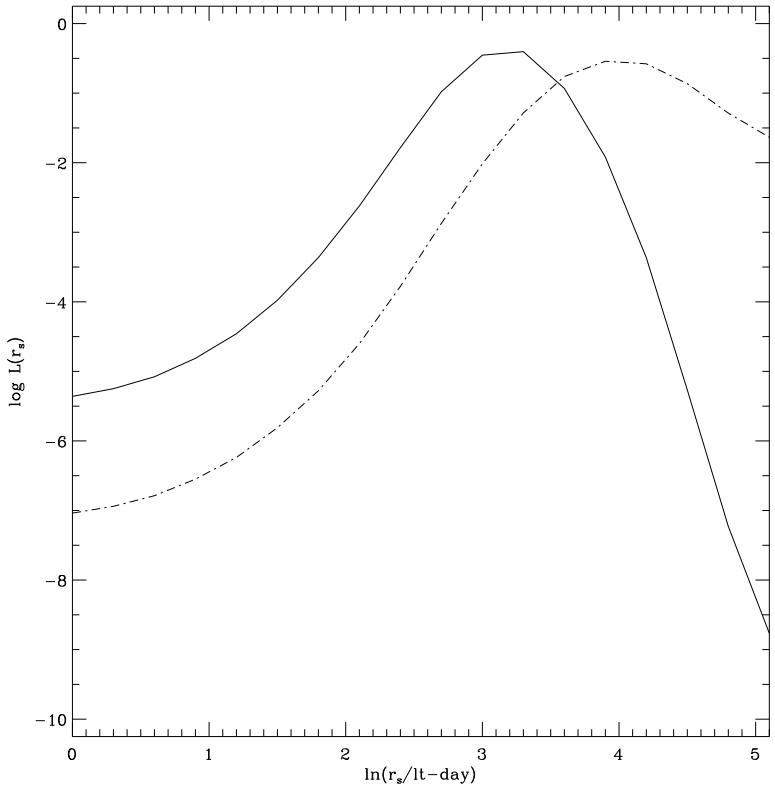

Fig. 6.— EG12: maximum likelihood curves for the size of the regions of high (solid) and low (dashed) ionization lines, respectively.

The problem with more complex models is that there is no simple, generally accepted structural model for the broad line region, and the initial results of the velocity-resolved RM experiments suggest that there may be no such common structure. As an experiment, we constructed a model consisting of an inner rotating disk and an outer spherical shell which dominates the core emission. We set the inner edge of the disk to $r_{disk,in} = 5$ light-days and left the outer edge $r_{disk,out}$ as the adjustable parameter. For simplicity we used a constant emissivity for the disk and a Keplerian rotation profile with an inner edge velocity of 10^4 km/s. The disk has an inclination of 45 degrees. For the spherical shell we adopted fixed inner and outer radii of $r_{sphere,in} = 60$ and $r_{sphere,out} = 160$ light-days respectively. For the shell we used a $v \propto 1/r^2$ velocity profile with a velocity of 5000 km/s at the inner edge. We normalized the models so that the disk contributes 20% of the flux at zero velocity, which also results in a single peaked line profile that resembles typical broad line profiles. We only carried out the calculations for a representative set of lens parameters ($\kappa_1 = \gamma_1 = 0.45$ and $\kappa_2 = \gamma_2 = 0.55$; see Mediavilla et al. 2009), but we now calculate Δm to correctly include the differential microlensing of the core and the wing. The final results for the outer radius of the disk component which dominates the wings of the line profile are $r_s = 50^{+40}_{-20}$ and $r_s = 70 \pm 30$ light-days the high and low ionization lines, respectively, where these are now 1σ uncertainties. While the model is somewhat arbitrary, the similarity of the results to the simpler analysis suggest that it was relatively safe to ignore the complexities.

5. DATA ANALYSIS

Mediavilla et al. (2009) collected from the literature the UV, optical and near-IR spectra shown in Figures 7 and 8 and summarized in Table 1. After excluding some of the noisier spectra used in Mediavilla et al. (2009), there were 18 pairs of lensed quasar images. The low ionization lines (CIII]λ1909, Mg IIλ2798, H$\beta\lambda$4861 and H$\alpha\lambda$6562) show a very good match of emission line profiles between images. For the high ionization lines[1] (OVI]λ1035, Lyα+NVλ1216, SiIV+OIVλ1400 and CIVλ1549), there are 5 examples where there are obvious differences in the line profiles: CIV in HE0435−1223DC, Lyα+NV in SBS0909+532, and Lyα+NV, SiIV+OIV] and CIV] in SDSS J1004+4112BA). SDSS J1004+4112 is a conspicuous example (Richards et al. 2004, Gómez-Álvarez et al. 2006, Lamer et al. 2006, Abajas et al. 2007, Motta et al. 2012), where a blue bump appears in several high ionization emission lines, as shown in Figure 1.

[1]EG12 included Lyα+NV in the high ionization group, as it has a similar RM lag as CIV (Clavel et al. 1991).

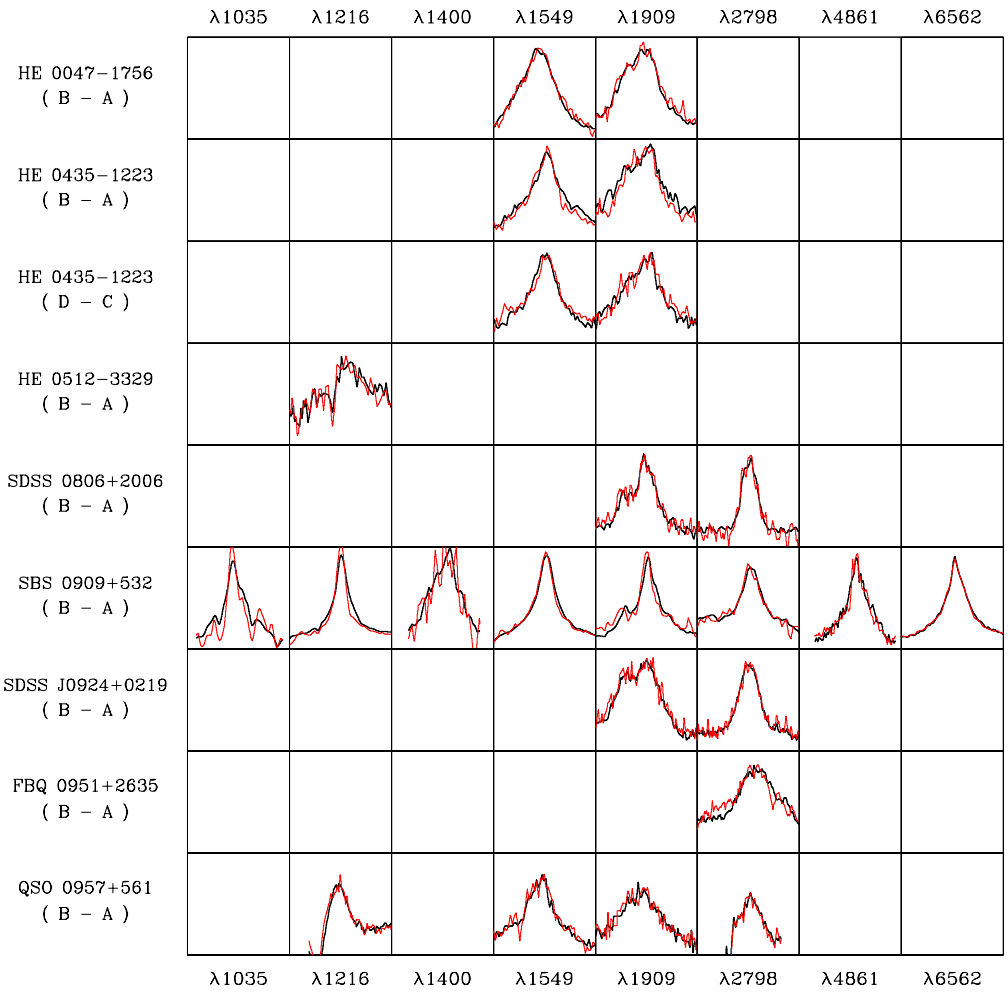

Fig. 7.— EG12: Emission line profiles for image pairs of several lens systems. Continuum-subtracted spectra were scaled to match the lines. Each emission line is plotted in the (-6000 km s^{-1}, 6000 km s^{-1}) range.

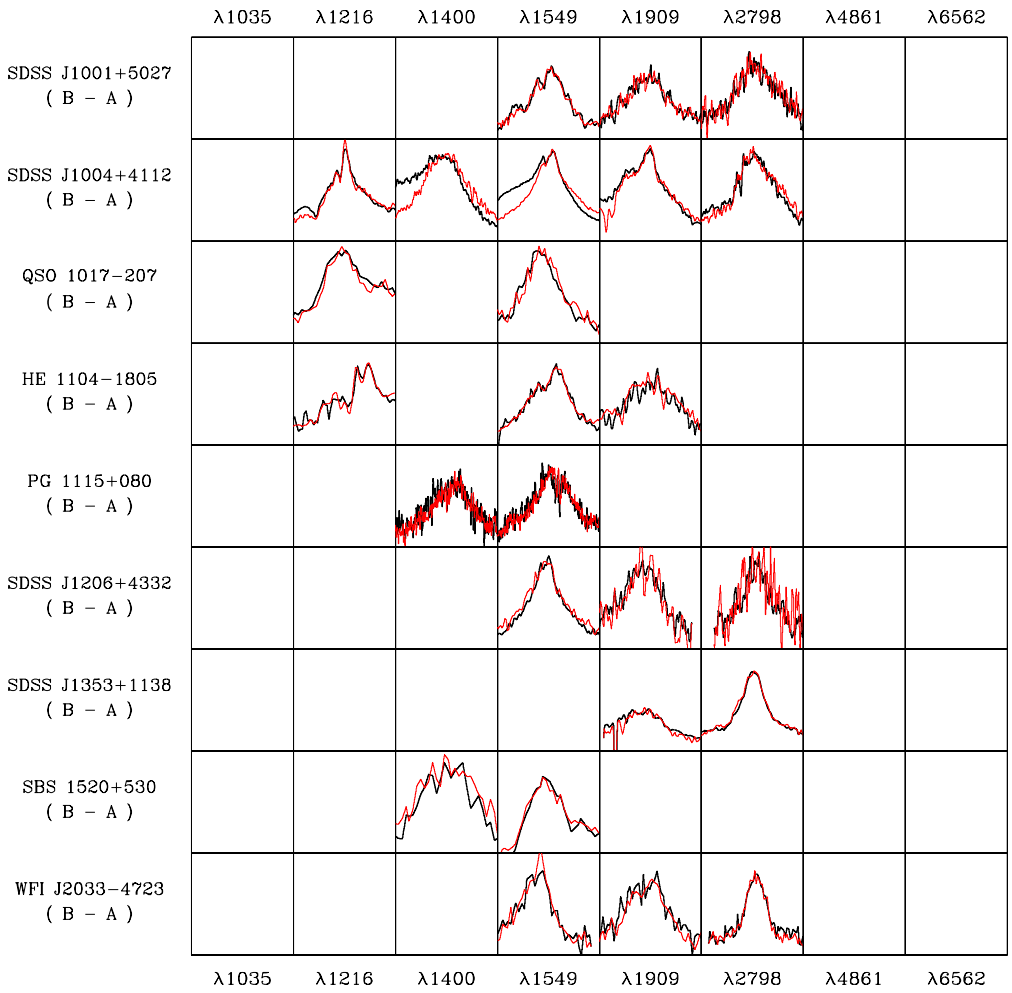

Fig. 8.— EG12: as in Fig. 7

Table 1: EG12: differential microlensing, $\triangle m_{core} - \triangle m_{wings}$, of the high and low ionization emission lines

Object (pair)	λ1035	λ1216	λ1400	λ1549	⟨ HIL ⟩	λ1909	λ2798	λ4861	λ6562	⟨ LIL ⟩
HE 0047–1756 (B-A)	-	-	-	+0.03	+0.03	+0.03	-	-	-	+0.03
HE 0435–1223 (B-A)	-	-	-	–0.21	–0.21	–0.19	-	-	-	–0.19
HE 0435–1223 (D-C)	-	-	-	+0.19	+0.19	+0.07	-	-	-	+0.07
HE 0512–3329 (B-A)	-	+0.04	-	-	+0.04	-	-	-	-	-
SDSS 0806+2006 (B-A)	-	-	-	-	-	+0.09	–0.26	-	-	–0.10
SBS 0909+532 (B-A)	–0.43	–0.23	-	–0.04	–0.18	–0.01	–0.02	–0.14	+0.00	–0.04
SDSS J0924+0219 (B-A)	-	-	-	-	-	+0.09	+0.09	-	-	+0.09
FBQ 0951+2635 (B-A)	-	-	-	-	-	-	+0.04	-	-	+0.04
QSO 0957+561 (B-A)	-	+0.03	-	+0.03	+0.03	+0.08	–0.13	-	-	–0.03
SDSS J1001+5027 (B-A)	-	-	-	–0.04	–0.04	+0.01	+0.04	-	-	+0.02
SDSS J1004+4112 (B-A)	-	–0.07	–0.29	–0.23	–0.20	–0.06	+0.02	-	-	–0.02
QSO 1017–207 (B-A)	-	–0.08	-	+0.15	+0.03	-	-	-	-	-
HE 1104–1805 (B-A)	-	+0.03	-	+0.02	+0.02	+0.03	-	-	-	+0.03
PG 1115+080 (A2-A1)	-	-	-0.10	–0.04	–0.07	-	-	-	-	-
SDSS J1206+4332 (A-B)	-	-	-	+0.17	+0.17	–0.12	+0.15	-	-	+0.01
SDSS J1353+1138 (A-B)	-	-	-	-	-	–0.16	+0.05	-	-	–0.06
SBS 1520+530 (B-A)	-	-	+0.19	+0.16	+0.18	-	-	-	-	-
WFI J2033–4723 (B-C)	-	-	-	–0.05	–0.05	–0.18	–0.14	-	-	–0.16

6. CONCLUSIONS

1. Consistent with recent studies (e.g. Sluse et al. 2011, 2012, Motta et al. 2012) EG12 found that the broad emission lines of gravitationally lensed quasars are weakly microlensed. We also find for the first time that high and low ionization lines appear to be microlensed differently, with higher magnifications observed for the higher ionization lines. This indicates that the emission regions associated with the high ionization lines are more compact, as would be expected from photoionization models. If we then make simple models of the microlensing effects, we obtain size estimates of $r_s = 24^{+22}_{-15}\sqrt{M/M_\odot}$ and $r_s = 55^{+150}_{-35}\sqrt{M/M_\odot}$ light-days for the high and low ionization lines. We also calculated the sizes for low ($L < 2 \times 10^{44}$ ergs s^{-1}) and high ($L > 2 \times 10^{44}$ ergs s^{-1}) luminosity sub-samples based on the magnification-corrected luminosity estimates from Mosquera & Kochanek (2011). For the low luminosity sub-sample we find $r_s = 16^{+11}_{-8}\sqrt{M/M_\odot}$ and $37^{+28}_{-18}\sqrt{M/M_\odot}$ light-days for the high and low ionization lines, while for the high luminosity sub-sample we find $r_s = 36^{+30}_{-14}\sqrt{M/M_\odot}$ and $r_s = 299^{+indet.}_{-103}\sqrt{M/M_\odot}$ light-days. While the uncertainties are too large to accurately estimate the scaling of the size with luminosity, the changes are consistent with the $L^{1/2}$ scaling expected from simple photoionization models.

2. Figure 9 compares these estimates to the results from the RM of local AGN using the uniform lag estimates by Zu et al. (2011) and the host galaxy-corrected luminosities of Bentz et al. (2009). This figure shows scaled EG12 estimates of r_s for microlenses of $M = 0.3M_\odot$. While the uncertainties in our microlensing estimates are relatively large, the agreement with the reveberation mapping results is striking. This is clearest for the low ionization lines which are the ones easily measured in ground-based RM campaigns, but the offset between the high and low ionization lines agrees with the offsets seen for the limited number of RM results

for high ionization lines. Fig. 9 also shows the estimated size of the CIV emission region for Q2237+030 by Sluse et al. (2011) which reveals a similar level of agreement. Because they were measuring the size of the higher velocity line components rather than the full line, the EG12 results should be somewhat smaller than the RM estimates for the full line. These results strongly suggest that the lensed quasars can provide an independent check of RM results and extend them to far more distant quasars relatively economically. Microlensing should also be able to address the controversies about lines like CIV which have few direct RM measurements but are crucial tools for studying the evolution of BHs at higher redshifts.

7. FUTURE WORK

With nearly 100 known lensed quasars, it's possible to expand the sample and begin making estimates of the size as a function of luminosity or other variables. Accurate estimates for individual quasars will require spectrophotometric monitoring, as in Sluse et al. (2011). As the BLRs are relatively large, the time scale for the variability is relatively long. A significant constraint can be gained for most of these lenses simply by obtaining one additional spectrum to search for changes over the years that have elapsed since archival spectra were taken. Lenses may also be good targets for RM studies at higher redshifts because the time delays of the images provide early warning of continuum flux changes and better sampling cadence of both the line and continuum for a modest investment of observing resources.

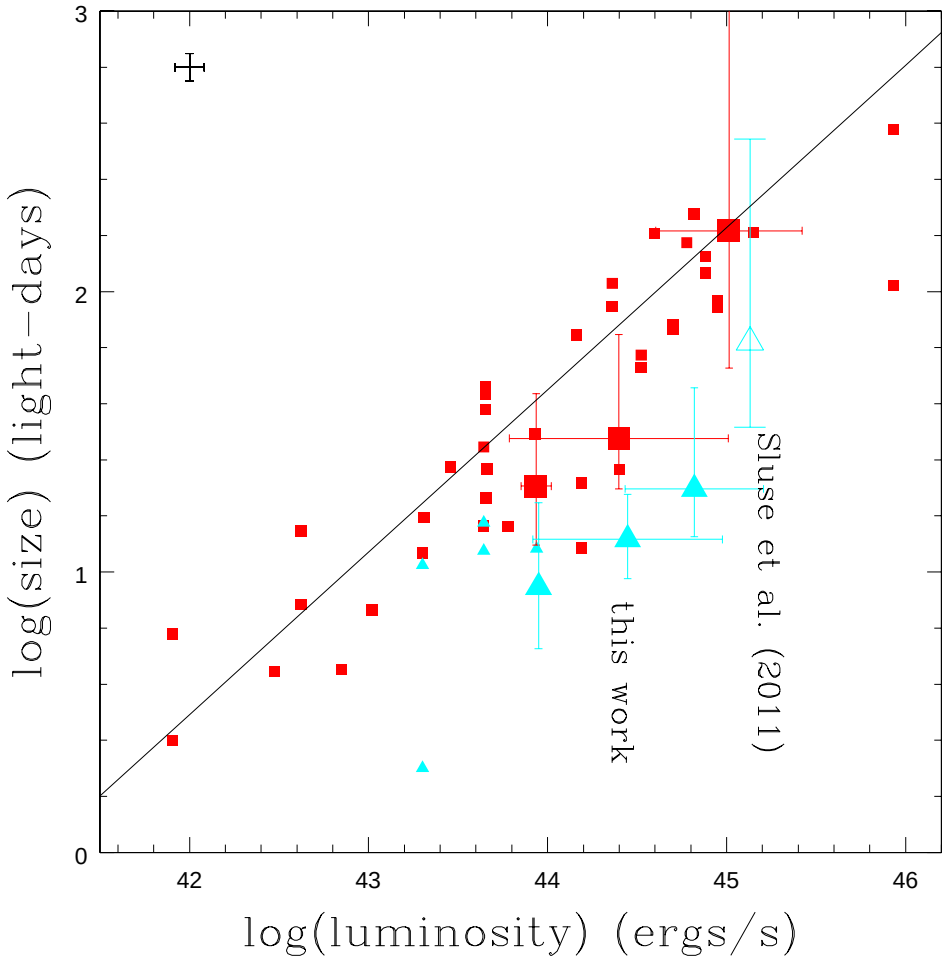

Fig. 9.— EG12: estimates of high (red) and low (blue) ionization BLR sizes as a function of quasar luminosity. EG12 (large solid triangles and squares) and Sluse et al. (2011) results for Q2237+0305 (large open triangle) with the magnification-corrected luminosity estimates of Mosquera & Kochanek (2011). The 3 large solid blue triangles (red squares) from EG12 correspond to the low, total and high luminosity subsamples defined in EG12for the high (low) ionization lines. The results from local RM appear as small triangles (high ionization lines) and squares (low ionization lines), using the uniform estimates of the lags by Zu et al. (2011) and the host-corrected luminosities from Bentz et al. (2009). The line is the best-fit correlation from Zu et al. (2011). The cross in the upper left corner shows the average uncertainty of the RM lag and the variance in the source luminosity during the mapping campaign.

REFERENCES

Abajas, C., Mediavilla, E., Muñoz, J. A., Popović, L. Č., & Oscoz, A. 2002, ApJ, 576, 640

Abajas, C., Mediavilla, E., Muñoz, J. A., Gómez-Álvarez, P., & Gil-Merino, R. 2007, ApJ, 658, 748

Assef, R. J., Denney, K. D., Kochanek, C. S., et al. 2011, ApJ, 742, 93

Barth, A. J., Nguyen, M. L., Malkan, M. A., et al. 2011, ApJ, 732, 121

Bentz, M. C., Peterson, B. M., Netzer, H., Pogge, R. W., & Vestergaard, M. 2009, ApJ, 697, 160

Bentz, M. C., Horne, K., Barth, A. J., et al. 2010, ApJ, 720, L46

Blackburne, J. A., Kochanek, C. S., Chen, B., Dai, X., & Chartas, G. 2011, arXiv:1112.0027

Brewer, B. J., Treu, T., Pancoast, A., et al. 2011, ApJ, 733, L33

Clavel, J., Reichert, G. A., Alloin, D., et al. 1991, ApJ, 366, 64

Dalal, N., & Kochanek, C. S. 2002, ApJ, 572, 25

Denney, K. D., Peterson, B. M., Pogge, R. W., et al. 2009, ApJ, 704, L80

Denney, K. D., Peterson, B. M., Pogge, R. W., et al. 2010, ApJ, 721, 715

Doroshenko, V. T., Sergeev, S. G., Klimanov, S. A., Pronik, V. I., & Efimov, Y. S. 2012, arXiv:1203.2084

Eigenbrod, A., Courbin, F., Sluse, D., Meylan, G., & Agol, E. 2008, A&A, 480, 647

Fine, S., Croom, S. M., Bland-Hawthorn, J., et al. 2010, MNRAS, 409, 591

Garsden, H., Bate, N. F., & Lewis, G. F. 2011, MNRAS, 418, 1012

Gómez-Álvarez, P., Mediavilla, E., Muñoz, J. A., et al. 2006, ApJ, 645, L5

Horne, K., Peterson, B.M., Collier, S., & Netzer, H. 2004, PASP 116, 465 - 476.

Jiménez-Vicente, J., Mediavilla, E., Muñoz, J. A., & Kochanek, C. S. 2012, ApJ, 751, 106

Keeton, C. R., Burles, S., Schechter, P. L., & Wambsganss, J. 2006, ApJ, 639, 1

Kollmeier, J. A., Onken, C. A., Kochanek, C. S., et al. 2006, ApJ, 648, 128

Lamer, G., Schwope, A., Wisotzki, L., & Christensen, L. 2006, A&A, 454, 493

Lewis, G. F., Irwin, M. J., Hewett, P. C., & Foltz, C. B. 1998, MNRAS, 295, 573

Lewis, G. F., & Ibata, R. A. 2004, MNRAS, 348, 24

MacLeod, C. L., Ivezić, Ž., Kochanek, C. S., et al. 2010, ApJ, 721, 1014

McLure, R. J., & Jarvis, M. J. 2002, MNRAS, 337, 109

Mediavilla, E., Muñoz, J. A., Lopez, P., et al. 2006, ApJ, 653, 942

Mediavilla, E., Muñoz, J. A., Falco, E., et al. 2009, ApJ, 706, 1451

Mediavilla, E., Muñoz, J. A., Kochanek, C. S., et al. 2011a, ApJ, 730, 16

Mediavilla, E., Mediavilla, T., Muñoz, J. A., et al. 2011b, ApJ, 741, 42

Metcalf, R. B., Moustakas, L. A., Bunker, A. J., & Parry, I. R. 2004, ApJ, 607, 43

Mortonson, M. J., Schechter, P. L., & Wambsganss, J. 2005, ApJ, 628, 594

Mosquera, A. M., & Kochanek, C. S. 2011, ApJ, 738, 96

Motta, V., Mediavilla, E., Muñoz, J. A., et al. 2002, ApJ, 574, 719

Motta, V., Mediavilla, E., Falco, E., & Munoz, J. A. 2012, arXiv:1206.1582

Nemiroff, R. J. 1988, ApJ, 335, 593

Netzer, H., Lira, P., Trakhtenbrot, B., Shemmer, O., & Cury, I. 2007, ApJ, 671, 1256

O'Dowd, M., Bate, N. F., Webster, R. L., Wayth, R., & Labrie, K. 2011, MNRAS, 415, 1985

Onken, C. A., & Kollmeier, J. A. 2008, ApJ, 689, L13

Pancoast, A., Brewer, B. J., Treu, T., et al. 2012, arXiv:1205.3789

Peterson, B. M. 1993, PASP, 105, 247

Peterson, B. M. 2006, Astronomical Society of the Pacific Conference Series, 360, 191

Poindexter, S., & Kochanek, C. S. 2010, ApJ, 712, 668

Richards, G. T., Keeton, C. R., Pindor, B., et al. 2004, ApJ, 610, 679

Schneider, P., & Wambsganss, J. 1990, A&A, 237, 42

Shen, Y., Greene, J. E., Strauss, M. A., Richards, G. T., & Schneider, D. P. 2008, ApJ, 680, 169

Sluse, D., Schmidt, R., Courbin, F., et al. 2011, A&A, 528, A100

Sluse, D., Hutsemékers, D., Courbin, F., Meylan, G., & Wambsganss, J. 2012, arXiv:1206.0731

Ulrich, M.-H., & Horne, K. 1996, MNRAS 283, 748 - 758

Vestergaard, M., & Peterson, B. M. 2006, ApJ, 641, 689

Wambsganss, J. 2006, Saas-Fee Advanced Course 33: Gravitational Lensing: Strong, Weak and Micro, 453

Wandel, A., Peterson, B. M., & Malkan, M. A. 1999, ApJ, 526, 579

Wayth, R. B., O'Dowd, M., & Webster, R. L. 2005, MNRAS, 359, 561

Zu, Y., Kochanek, C. S., & Peterson, B. M. 2011, ApJ, 735, 80